Quantitative uncertainty determination of phase retrieval in RABBITT

JIA-BAO JI,* SAIJOSCHA HECK, MENG HAN, AND HANS JAKOB WÖRNER

Laboratorium für Physikalische Chemie, ETH Zürich, Vladimir-Prelog-Weg 2, 8093 Zürich, Switzerland
*Jiabao.Ji@phys.chem.ethz.ch

Abstract: Reconstruction of attosecond beating by interference of two-photon transitions (RABBITT) is one of the most widely used approaches to measure the time delays in photoionization. The time delay, which corresponds to a phase difference of two oscillating signals, is usually retrieved by cosine fitting or fast Fourier transform (FFT). We propose two estimators for the phase uncertainty of cosine fitting from the signal *per se* of an individual experiment: (i) $\sigma(\varphi_{\text{fit}}) \approx \frac{B}{A}\sqrt{\frac{2}{N}}$, where B/A is the mean-value-to-amplitude ratio, and N is the total count number, and (ii) $\sigma(\varphi_{\text{fit}}) \approx \sqrt{\frac{1-R^2}{R^2 n_{\text{bins}}}}$, where n_{bins} is the total number of bins in the time domain, and R^2 is the coefficient of determination. The former estimator is applicable for the statistical fluctuation, while the latter includes the effects from various uncertainty sources, which is mathematically proven and numerically validated. This leads to an efficient and reliable approach to determining quantitative uncertainties in RABBITT experiments and evaluating the observed discrepancy among individual measurements, as demonstrated on the basis of experimental data.

1. Introduction

1.1. RABBITT experiment

Our physical world evolves on many different timescales. The typical period of the electron motion in atoms or molecules is in the sub-femtosecond, i.e. attosecond (as, 1 as = 10^{-18} s) range, which corresponds to $T = h/\Delta E$, where the involved energy intervals are $1 \sim 100$ eV. In order to capture such ultrafast dynamics, one needs an ultrafast signal source and a corresponding detection scheme. This is achieved by attosecond extreme-ultraviolet (XUV) light or X-ray pulses generated by high-harmonic generation (HHG) [1,2] or free-electron lasers (FELs) [3,4]. The pulses can be either comb-like attosecond pulse trains (APTs) [5,6] or single attosecond pulses (SAPs) [7]. The dynamical information is extracted by pump-probe schemes that correlate the photoelectron spectra and the pump-probe time delays, where the attosecond XUV (or X-ray) pulse is the pump and a femtosecond infrared (IR) pulse serves as the probe. The schemes for APTs and SAPs are RABBITT [8–11] and attosecond streaking [12–16], respectively. In this paper, we focus on the RABBITT technique, where cosine-like beating signals are observed and the electron's dynamics is characterized by the phase difference of two signals. We expect that the proposed methods can be readily generalized to the $\omega - 2\omega$ *in-situ* methods [17], PROOF [16], and possibly other interferometric methods.

The origin of the beating pattern is known as the interference of different XUV-IR transition pathways [18–20]. In short, the same observed photoelectron kinetic energy corresponds to the absorption of one HHG-XUV photon and the exchange of $\pm m$ IR photons, where plus and minus correspond to absorption and emission, respectively. The transition amplitude of the m-pathway reads:

$$\mathcal{A}_{(q;m)} = \mathcal{E}_{\text{IR}}^m \mathcal{E}_{q-m} \mathcal{M}_{(q;m)}, \tag{1}$$

where $\mathcal{E}_{IR}$ and $\mathcal{E}_{q-m}$ denote the amplitudes of the dressing IR field and the $(q - m)$-order HHG, and $\mathcal{M}_{(q;m)}$ is the corresponding matrix element that contributes to the q-th HHG band. If several sub-pathways contribute to the m-pathway *coherently* [19,21], then $\mathcal{M}_{(q;m)}$ is the sum of those elements. The phase $\arg(\mathcal{E}_{IR}) = \omega\tau$ is referenced to the XUV pulse, where a greater τ indicates that the dressing IR pulse has a shorter optical path length.

Let us recall the well-known electron two-slit interference experiment [22], where the electrons are detected one-by-one, and the interference of the wave function is presented by the beating *probability* of finding the electron as a function of position on the screen. In the RABBITT experiment, the observed signal is proportional to the probability density function (PDF) oscillating along the time axis (XUV-IR delay), and the pattern builds up while the number of detected electrons increases. For an APT containing only odd-order harmonics, the even-order sidebands (SBs) correspond to the process where m is an odd number. The q-SB signal for a single atom or molecule can be described by:

$$S_q = \left| \sum_m \mathcal{A}_{(q;m)} \right|^2.$$ (2)

Figure 1(a) illustrates possible pathways with $m = \pm1, \pm3$ for an even-order harmonic SB, which lies between two mainbands (MBs) of the XUV pulse. The high-$|m|$ pathways become important under a strong dressing field [23]; the $m = \pm2$ pathways can be selectively enabled by a double-frequency dressing field [21,24,25]. There are also reports on conducting RABBITT with HHG frequencies separated by 1ω or 3ω [3,26,27]. Here we present the analysis mainly based on the interference between $m = \pm1$ pathways, but the methods are applicable to other schemes. In our case, Eq. (2) is simplified to:

$$
\begin{aligned}
S_q &= \left| \mathcal{A}_{(q;1)} + \mathcal{A}_{(q;-1)} \right|^2 \\
&= |\mathcal{A}_{(q;1)}|^2 + |\mathcal{A}_{(q;-1)}|^2 + 2|\mathcal{A}_{(q;1)}||\mathcal{A}_{(q;-1)}| \cos\left[\arg(\mathcal{A}_{(q;1)}) - \arg(\mathcal{A}_{(q;-1)}) \right].
\end{aligned}
$$ (3)

Detailed analysis of the SBs' intensities can be found in Ref. [28]. The argument of the cosine function in Eq. (3) can be expressed as:

$$\arg(\mathcal{A}_{(q;1)}) - \arg(\mathcal{A}_{(q;-1)}) = 2\omega(\tau - \tau_{XUV} - \tau_A),$$ (4)

where τ_{XUV} is known as "attochirp" [29–31] and τ_A is the ionization time, which consists of the bound-continuum part τ_{bc} and the continuum-continuum part τ_{cc} [19,20,32–34]. Instead of the absolute value of τ_A, experiments measure $\Delta\tau_A$ between a reference channel and one or several target channel(s) as the relative ionization time delay(s) [35]. Figure 1(b) shows the experimental data from argon (Ar), where the oscillations on different bands along the pump-probe time delay axis are clearly visible. In interference between $m = \pm1$ and $m = \mp3$ pathways results in the 4ω-oscillation, which is observed by subtracting the 2ω-component from the RABBITT signal or from the FFT spectrum, as demonstrated in Fig. 2. Note that we have integrated the signal within the energy range of each SB, while it is possible to extract the time delays as a function of the electron kinetic energy, such as the Rainbow technique [36,37], which reveals the energy-dependent phase variation [38], or the global complex-amplitude fitting method [39–41], which is suitable for overlapping or congested bands. Its uncertainty analysis can be performed under the principles introduced in this article with extended mathematical considerations, which is currently in progress.

1.2. Uncertainty of the measured time delay

The determination of the time delay relies on the phase retrieval of the signal, and it is important to obtain the uncertainty of the measurement. According to the Joint Committee for Guides in
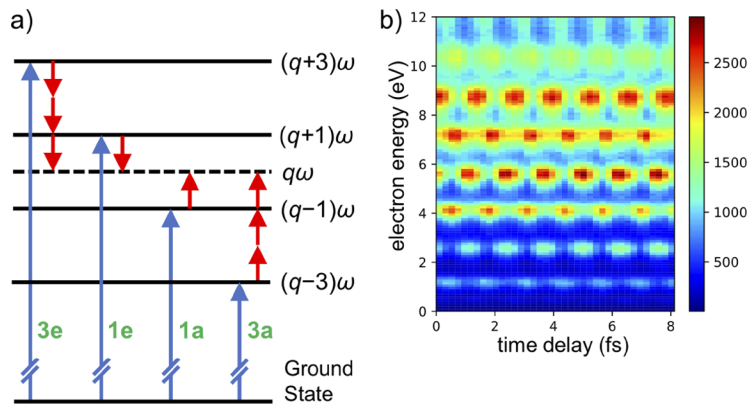
Fig. 1. (a) Schematic of RABBITT: $q\omega$ (dashed line) refers to the q-th sideband, while the solid lines refer to the XUV bands of the photoelectron spectrum. The blue and red arrows refer to XUV and IR photons, respectively. For clarity, only one sideband is illustrated with four contributing pathways: emitting 3 IR photons (3e), emitting 1 IR photon (1e), absorbing 1 IR photon (1a), and absorbing 3 IR photons. (b) Experimental data of Ar, where the photoelectron bands are aligned to $q = 14$ in (a).
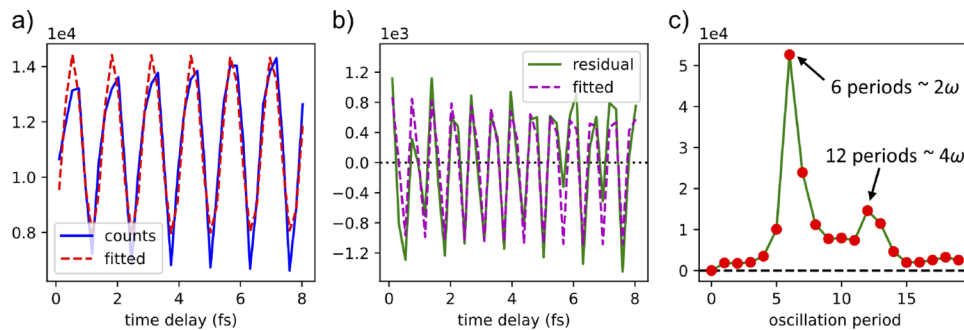

Fig. 2. Observation of the 4ω-component in a typical RABBITT signal. (a) Experimental counts (blue solid) and cosine fitting with 2ω (red dashed). (b) The residual of the 2ω-cosine-fitting (green solid) and the 4ω-cosine fitting of the residual (magenta dashed). (c) FFT of the RABBITT signal (with background subtracted).

Metrology (JCGM), the uncertainty determination is categorized into two types: (A) evaluated by statistical methods, and (B) evaluated by other means [42–44]. In practice, the Type A uncertainty is the discrepancy among individual outcomes, and Type B uncertainty reflects the precision for each measurement. For attosecond science specifically, the outcome is sensitive to experimental conditions (e.g. the environment for XUV generation, pump-probe overlap in space and time, jitter of the delay stage, noise of the detector). Reference [31] discusses the uncertainty caused by the attochirp, and a comprehensive study of the contributing factors can be found in Ref. [35]. In general, the imperfect control of conditions can either (I) shift the expected value of the desired attosecond time delay by an amount related to specific experimental conditions, or (II) blur the oscillation pattern without changing the expected value; here the "expected value" is a conceptual limit of the average of repeating a measurement an *infinite number of times* under *exactly* the same conditions. The effect (I) may cause systematic error compared with experiments under better control of the conditions, while the effect (II) results in unequal precision of individual measurements. Qualitative or semi-quantitative estimations of single-measurement precision with corresponding weighting schemes have been applied in previous studies [14,40,41,45–51],

which yields the Type A uncertainty of the studied experiments. However, to the best of our knowledge, no explicit formula has been proposed for determining the Type B uncertainty, namely, the uncertainty of a single measurement. The Type B uncertainty is meaningful when the number of individual experiments is comparatively small [42]. Furthermore, if the Type A uncertainty is much greater than the Type B uncertainty, it is an indication of the effect (I) discussed above, which provides hints for optimizing the experimental conditions.

1.3. Outline of this article

Here we propose two individual estimators based on the experimental signal *per se*: the B/A-estimator (Sec. 3) and the R^2-estimator (Sec. 4). We explicitly consider four effects: statistical fluctuations, smearing effect, shifting effect, and background noise, which finally fall into three categories (Sec. 2). The derived estimators are manifested by numerical simulations (Sec. 5), where the two estimators are compared. The relation between cosine fitting and FFT can be found in Sec. 6. The individual uncertainty leads to a weighting scheme (Sec. 7), where we introduce the S-value to quantify the consistency between the Type A and Type B uncertainties. Finally, in Sec. 8, we present a pair of examples from experimental data to demonstrate how one knows from the S-value whether the expected value of the time delay may be subjected to the experimental conditions on an unresolved degree of freedom.

2. Statistical fluctuations, smearing effect, shifting effect, and background noise

Experimentally, the detected electrons are binned by the step size of the delay time, and the number of counts in each bin F_i obeys a Poisson distribution; when the count number is large enough ($\gtrsim 10$), the distribution can be approximated by normal distribution with variance equal to the mean value [52]

$$F_i \sim \mathcal{N}(f(t_i), f(t_i)), \tag{5}$$

where

$$f(t_i) = A\cos(2\omega t_i + \varphi) + B \tag{6}$$

is the PDF integrated over the time bin, which is approximately the PDF multiplied by the bin width, and t_i is the central time of the i-th bin. A is a positive real number, and we define $T = \pi/\omega$ as the oscillation period of the signal. Equation (5) therefore gives the statistical fluctuation of the signal.

In the derivation of Eq. (1), we have assumed that different pathways contribute coherently. In reality, the system undergoes partial *decoherence*, where pathways are mixed incoherently, and the total PDF is the sum of individual PDFs. The decoherence can be characterized by reconstructing the density matrix, and the origin of decoherence includes the spatial variation of the electric field, scattering of the ejected electrons, imperfect detector, and so on [53]. For RABBITT experiments, the decoherence (referred as the smearing effect) occurs both spatially and temporally.

The spatial smearing effect is related to the fact that the PDF is integrated over the focal volume. Mismatches in the XUV and IR focal-spot sizes, imperfect overlap, different Rayleigh lengths and the focusing of different harmonic orders at different positions along the propagation direction, among others, contribute to this effect, which can be expressed as a spatial variation of the amplitudes and phases:

$$f(t) = \int A(\mathbf{r})\cos[2\omega t + \varphi(\mathbf{r})] + B(\mathbf{r})d^3\mathbf{r}, \tag{7}$$

where we assume interference within a small volume of $d^3\mathbf{r}$, and $A(\mathbf{r})$, $B(\mathbf{r})$, and $\varphi(\mathbf{r})$ correspond to Eqs. (3) and (4) with position-dependent coefficients. Comparing Eq. (7) with Eq. (6), we

have:

$$Ae^{i\varphi} = \int A(\mathbf{r})e^{i\varphi(\mathbf{r})}d^3\mathbf{r}, \quad B = \int B(\mathbf{r})d^3\mathbf{r}, \tag{8}$$

and $A \leq \int A(\mathbf{r})d^3\mathbf{r}$, where the equal sign holds only when $\varphi(\mathbf{r})$ is constant over the whole focal volume. Moreover, if the focal volume varies among individual experiments, the expected value of φ may change, as the effect (I) discussed in Sec. 1.2. Nevertheless, if channels from the same SB are compared to retrieve the relative time delays $\Delta\tau_A$, this effect is largely cancelled.

The temporal smearing effect arises from the inaccuracy of defining the XUV-IR delay. Specifically, we consider the following scenarios: (i) the delay stage position is binned by the step size; (ii) the delay stage jitters randomly between the sequential electrons being detected; (iii) there is shot-to-shot XUV-IR phase jitter due to the fluctuation of generation conditions, and we assume each photoelectron originates from a different shot; (iv) if multiple scans are superimposed, there can be a long-term drift of the path length caused by thermal expansion. There can be other sources of temporal inaccuracy, but they are generalized by a redistribution function $D(\tau)$ that is normalized to 1, which describes the probability that the time delay is recorded as t but the true value should be $t + \tau$. Its effect on the PDF is expressed by convolution:

$$f_{\text{smeared}}(t) = \int_{-\infty}^{+\infty} f(t+\tau)D(\tau)d\tau = \int_{-\infty}^{+\infty} f(t-\tau)\bar{D}(\tau)d\tau = (f * \bar{D})(t), \tag{9}$$

where $D(\tau)$ is the redistribution function, and $\bar{D}(\tau) = D(-\tau)$. Equations (6) and (9) give:

$$f_{\text{smeared}}(t) = \left[\mathscr{F}\{\bar{D}\}(2\omega)\right] \cdot A\cos(2\omega t + \varphi) + B = A'\cos(2\omega t + \varphi) + B, \tag{10}$$

which is a cosine signal with the same mean value and phase, but reduced amplitude by a factor of the Fourier transform of the redistribution function. For (i) and (iv), $D(\tau) = \frac{1}{\Delta t}\text{rect}\left(\frac{\tau}{\Delta t}\right)$ is a rectangular function, and $\frac{A'}{A} = \text{sinc}\left(\frac{\Delta t}{T}\right)$, where Δt is the bin width or the drift range, respectively. For (ii) and (iii), we can assume the jitter obeys normal distribution $\mathcal{N}(0, \sigma_\tau^2)$, and $\frac{A'}{A} = \exp\left[-2\pi^2\left(\frac{\sigma_\tau}{T}\right)^2\right]$. Therefore, the smearing effects are fully characterized by the signal-to-noise ratio, or equivalently, the B/A ratio.

The shifting effect refers to the correlated jitter, where *all* counts in the i-th bin are recorded as a delay-stage position that deviates $\Delta t_i = \eta_i/(2\omega)$ from the true value. This is relevant when multiple detected electrons are from the same shot, or at least between the typical timescale within which the jitter randomizes, which are denoted as a *batch* of electrons in the following discussion. The change of counts yields:

$$\Delta F_i = A\left[-\sin(2\omega t + \varphi)\eta_i - \frac{1}{2}\cos(2\omega t + \varphi)\eta_i^2 + O(\eta_i^3)\right]. \tag{11}$$

If $\Delta t_i \sim \mathcal{N}(0, \sigma_s^2)$, then to the lowest order,

$$\Delta F_i \sim \mathcal{N}\left(0, A^2\sigma_\eta^2\right), \tag{12}$$

where $\sigma_\eta = 2\omega\sigma_s = 2\pi\sigma_s/T$. Large shifting destroys the oscillating pattern, while ellipse-specific fitting can still retrieve the phase difference between two channels [3,54]; this is named "timing-jitter unaffected RABBITT time delay extraction method" (TURTLE) [55]. Our work on combining TURTLE with cosine fitting is in progress. Note, however, that we have used an implicit assumption that the number of electrons in a batch is the same as the binned value, which

decreases for finer binning. If we assume that the average number of electrons in a batch, denoted as b, depends on the pulse intensity and the randomization of the jitter but does not depend on the step size, then a finer bin contains fewer batches. Let $\kappa = N/(b \cdot n_{\text{bins}})$ be the average number of independent batches that each bin contains. The standard deviation (std) of the shift of the bin (each batch contributes $1/\kappa$ to the bin) becomes:

$$\sigma_{\text{s}} = \sigma_{\text{batch, s}}/\sqrt{\kappa}, \quad \sigma_{\eta} = \sigma_{\text{batch, }\eta}/\sqrt{\kappa}. \tag{13}$$

Furthermore, the detector may have a background noise (approximately white noise) with variance of $\sigma^2_{\text{noise}} = \gamma B$. The fluctuation, shifting, and background noise are assumed to be independent uncertainty sources. Overall, we have $B/A \geq 1$, where the equality is reached only when the signal has $|\mathcal{A}_{(q;1)}| = |\mathcal{A}_{(q;-1)}|$ defined in Eq. (3) and no smearing effect, shifting effect, or background noise arises.

3. Cosine fitting for the binned histogram and the B/A-estimator

The RABBITT signal is fitted by a cosine function, which can be equivalently written as the linear decomposition into three parts:

$$F_{\text{fit}}(t_i) = B_{\text{fit}} + \alpha \cos(2\omega t_i) + \beta \sin(2\omega t_i) = B_{\text{fit}} + A_{\text{fit}} \cos(2\omega t_i + \varphi_{\text{fit}}), \tag{14}$$

where for integer number of oscillation periods,

$$B_{\text{fit}} = \frac{\sum_i F_i}{n_{\text{bins}}}, \quad \alpha = \frac{\sum_i \cos(2\omega t_i)F_i}{n_{\text{bins}}/2}, \quad \beta = \frac{\sum_i \sin(2\omega t_i)F_i}{n_{\text{bins}}/2}, \tag{15}$$

and $\varphi_{\text{fit}} = -\arctan(\beta/\alpha)$. For non-integer number of periods, B_{fit}, α, and β are given by formulae in the Supplement 1 (Ref. [56]). Here we have assumed the oscillation period is perfectly fitted from the reference channel; the effects of the deviation of the fitted T will be discussed in Sec. 6. Assuming that the deviations of different bins are uncorrelated, we have the expected values:

$$\text{Ex}(A_{\text{fit}}) \approx A'\left[1 - 2\pi^2\left(\frac{\sigma_{\text{s}}}{T}\right)^2\right], \quad \text{Ex}(B_{\text{fit}}) = B, \tag{16}$$

where A' is defined by Eq. (10) and is denoted as A in the following discussion. $\text{Ex}(\alpha) = \text{Ex}(A_{\text{fit}})\cos\varphi$, $\text{Ex}(\beta) = -\text{Ex}(A_{\text{fit}})\sin\varphi$, and $\text{Ex}(\varphi_{\text{fit}}) = \varphi$. The variances and the correlation of α and β are:

$$\text{Var}(\alpha) = \sum_i \frac{\cos^2(2\omega t_i)}{n^2_{\text{bins}}/4}\text{Var}(F_i) \approx \frac{\int_0^{n_T T}\cos^2(2\omega t)\text{Var}(\varepsilon;t)\text{d}t}{n_T T n_{\text{bins}}/4},$$

$$\text{Var}(\beta) \approx \frac{\int_0^{n_T T}\sin^2(2\omega t)\text{Var}(\varepsilon;t)\text{d}t}{n_T T n_{\text{bins}}/4}, \tag{17}$$

$$\text{Cov}(\alpha, \beta) \approx \frac{\int_0^{n_T T}\sin(2\omega t)\cos(2\omega t)\text{Var}(\varepsilon;t)\text{d}t}{n_T T n_{\text{bins}}/4}.$$

The propagation of uncertainty yields:

$$\text{Var}(\varphi_{\text{fit}}) \approx \frac{1}{A^2}\left[\sin^2\varphi\text{Var}(\alpha) + \cos^2\varphi\text{Var}(\beta) + 2\sin\varphi\cos\varphi\text{Cov}(\alpha, \beta)\right]. \tag{18}$$

Without loss of generality, we suppose the PDF has $\varphi = 0$. We use integer number of periods (n_T) for mathematical proofs, which is extended to non-integer values by numerical simulations

in Sec. 5. Then Eq. (18) is simplified to:

$$\text{Var}(\varphi_{\text{fit}}) \approx \frac{1}{A^2} \frac{\frac{1}{\pi} \int_0^{2\pi} \sin^2 \xi \text{Var}(\varepsilon; \xi) d\xi}{n_{\text{bins}}/2}, \tag{19}$$

where $\xi = 2\omega t$. The random variable $\varepsilon(t)$ includes all uncertainty sources mentioned above:

$$\varepsilon(t_i) := F_i - F_{\text{fit}}(t_i) \sim \mathcal{N}(0, \text{Var}(\varepsilon; t_i)). \tag{20}$$

Different types of uncertainty, their integrals, and the contributions to $\text{Var}(\varphi_{\text{fit}})$ are listed in Table 1, where $N = B \cdot n_{\text{bins}}$ is the total count number. Independent sources of uncertainty (s) are combined by simple addition:

$$\text{Var}_{\text{total}}(\varepsilon; \xi) = \sum_s \text{Var}_s(\varepsilon; \xi). \tag{21}$$

The B/A ratio is independent of N or n_{bins} and can easily be obtained from the signal *per se* ($A_{\text{fit}} \approx A$ when shifting is not very large). If the statistical fluctuation is the main uncertainty
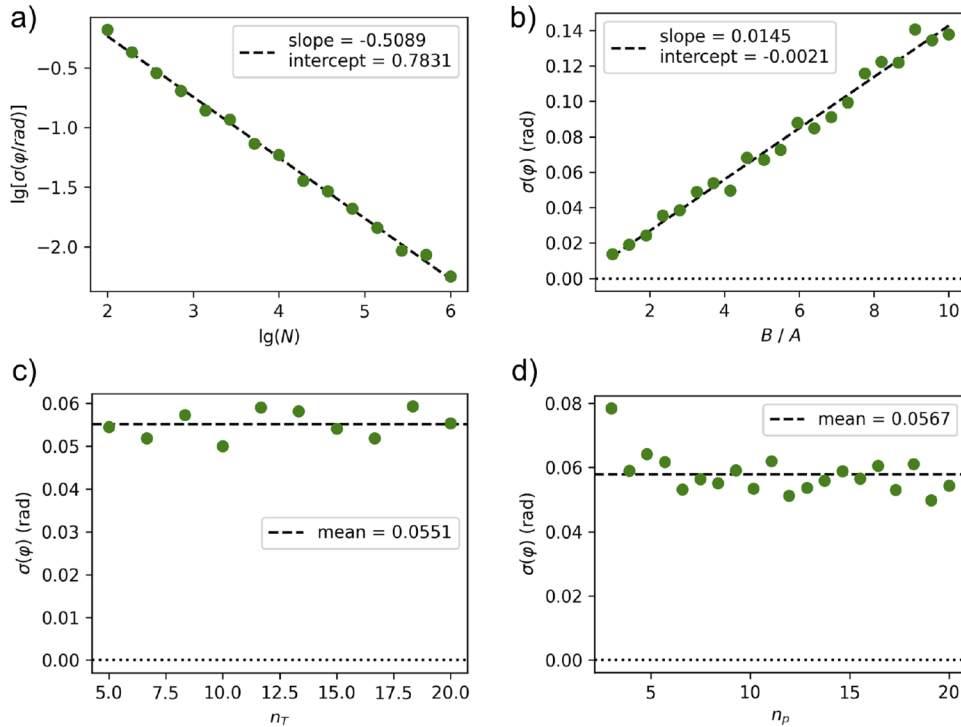

Fig. 3. Simulated RABBITT signals are generated with $N = 10^4$, $B/A = 4.0$, $n_T = 5$, $n_p = 10$. Each simulation scans one parameter. The standard deviation of fitted φ is calculated based on 100 independent trials for each green circle. (a) Scan over N (in logarithm scale); in theory, the slope is -0.5 and the intercept is 0.7526. (b) Scan over B/A ratio; in theory, the slope is 0.0141 and the intercept is 0. (c) Scan over n_T (with interval of 5/3); the expected $\sigma(\varphi) = 0.0566$. (d) Scan over n_p (with interval of 17/19); the expected $\sigma(\varphi) = 0.0566$, and the binning effect is only significant for $n_p = 3$.

Table 1. Different Types of Random Variables $\varepsilon(t)$, their Integrals of the Variances, and the Contributions to the Variance of φ_{fit}

Type	$\text{Var}(\varepsilon; \xi)$	$\frac{1}{\pi} \int_0^{2\pi} \frac{1}{2} \text{Var}(\varepsilon; \xi) d\xi$	$\frac{1}{\pi} \int_0^{2\pi} \sin^2 \xi \text{Var}(\varepsilon; \xi) d\xi$	$\text{Var}(\varphi_{\text{fit}})$
Poisson	$A\cos\xi + B$	B	B	$\frac{2}{N}\left(\frac{B}{A}\right)^2$
Background	γB	γB	γB	$\frac{2\gamma}{N}\left(\frac{B}{A}\right)^2$
Shifting	$A^2 \sigma_\eta^2 \sin^2 \xi$	$\frac{1}{2} A^2 \sigma_\eta^2$	$\frac{3}{4} A^2 \sigma_\eta^2$	$\frac{3b}{2N}\sigma_{\text{batch}}, \eta^2$

source, the phase fitting uncertainty has a concise expression:

$$\sigma(\varphi_{\text{fit}}) \approx \frac{B}{A}\sqrt{\frac{2}{N}}. \tag{22}$$

In this case, the phase retrieval precision is proportional to $N^{-1/2}$, which agrees with the previous study [35]; it is also independent of n_{bins}, as shown in Fig. 3 (see Sec. 5 for details). The background noise increases the std of φ_{fit} by a factor of $(1 + \gamma)^{1/2}$. The contribution of the shifting effect is $\frac{3}{2n_{\text{bins}}}\sigma_\eta^2 = \frac{3}{2n_{\text{bins}}}\sigma_{\text{batch}}, \eta^2/\kappa = \frac{3b}{2N}\sigma_{\text{batch}}, \eta^2$, which ultimately depends on N instead of n_{bins}, as numerically verified in Sec. 5.

4. R^2-estimator

The determination of the background noise and the shifting effect needs *a priori* knowledge of γ and σ_η. However, the combined uncertainty can be estimated by the coefficient of determination defined as [57]:

$$R^2 := 1 - \frac{\sum_i \left[F_i - F_{\text{fit}}(t_i)\right]^2}{\sum_i (F_i - \langle F \rangle)^2} \approx 1 - \frac{\int_0^{2\pi} \left[\varepsilon(\xi)\right]^2 d\xi}{\int_0^{2\pi} \left[A \cos \xi + \varepsilon(\xi)\right]^2 d\xi}, \tag{23}$$

where $\langle F \rangle$ is the mean value of F_i. The R^2-value describes the closeness between the signal and the fitted model; for an ideal cosine signal, $R^2 = 1$. The expectation value of R^2 yields:

$$\text{Ex}\left(R^2\right) = \frac{\int_0^{2\pi} \text{Var}(\varepsilon; \xi) d\xi}{\pi A^2 + \int_0^{2\pi} \text{Var}(\varepsilon; \xi) d\xi}. \tag{24}$$

Therefore, the R^2-estimator is expected to be:

$$\text{Ex}\left(\frac{1 - R^2}{R^2 n_{\text{bins}}}\right) = \frac{1}{A^2} \frac{\frac{1}{\pi} \int_0^{2\pi} \frac{1}{2}\text{Var}(\varepsilon; \xi) d\xi}{n_{\text{bins}}/2}. \tag{25}$$

Comparing Eq. (25), Eq. (19), and the integrals in Table 1, we find that for the Poisson-like and background (constant white noise) $\varepsilon(t)$, the R^2-estimator is unbiased, while for the shifting effect, the R^2-estimator is smaller by a factor of 2/3. With Eq. (21), the std of φ_{fit} with multiple sources of uncertainty lies between the lower and upper boundaries:

$$\sqrt{\frac{1 - R^2}{R^2 n_{\text{bins}}}} \le \sigma(\varphi_{\text{fit}}) \le \sqrt{\frac{3}{2}} \sqrt{\frac{1 - R^2}{R^2 n_{\text{bins}}}}. \tag{26}$$

Although Eq. (26) formally depends on n_{bins}, it does not contradict Eq. (22) when the statistical fluctuation dominates the total uncertainty, since at given N, R^2 decreases for larger n_{bins}, as shown in Supplement 1.

5. Validation by numerical simulations

5.1. B/A-method

Simulated RABBITT signals are generated by the accept-reject algorithm [58], and the detailed method is given in Supplement 1. In order to verify Eq. (22), the total count number N, the B/A ratio, the number of oscillation periods n_T, and the bins per period n_p are scanned, which perfectly agrees with the expression, as shown in Fig. 3. Note that the relation also holds for non-integer n_p or n_T.

5.2. R^2-method

Figure 4 manifests that the upper limit in Eq. (26) is precise for an ideal signal that is only subject to the shifting effect with small jitter. The simulated $\sigma(\varphi_{\text{fit}})$ falls between the two limits up to $\sigma_s/T \sim 0.4$. Note that for white noise [59], $\sigma(\varphi_{\text{fit}}) = \pi/\sqrt{3} \approx 1.81$, which corresponds to uniform distribution, while the lower limit of Eq. (26) gives $\sqrt{\pi/2} \approx 1.25$, because $R^2 n_{\text{bins}} \sim \chi^2(k = 2)$. This corresponds to the plateaus in Fig. 4(b).
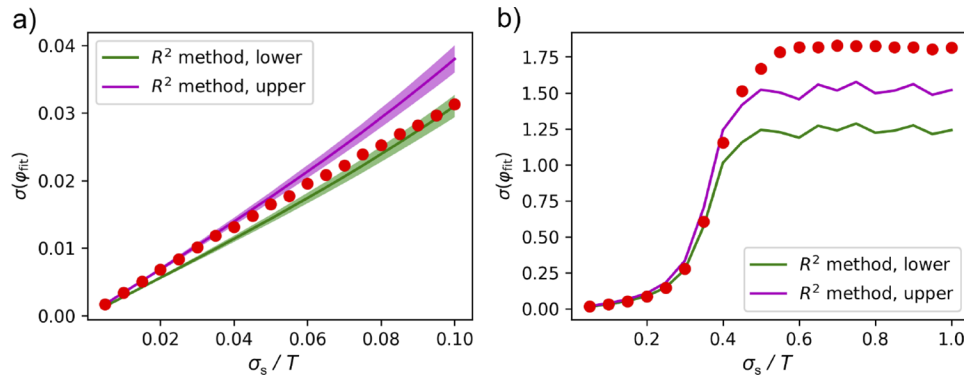

Fig. 4. Correlated jitter of an ideal signal with $n_{\text{bins}} = 500$. Each red circle corresponds to 5000 independent trials. The line and shadow indicate the mean value and standard deviation of the estimated $\sigma(\varphi_{\text{fit}})$ for each trial, respectively. (a) shows the small-σ_s regime, while (b) shows the large-σ_s regime.

Figure 5 shows the effects of various uncertainty sources on the simulated RABBITT signals and compares the uncertainty predicted by the B/A- and the R^2-estimators based on each independent trial. It is clear that Eq. (22) underestimates the uncertainty unless the statistical fluctuation is the main uncertainty source compared with correlated jitter (Fig. 5(a) and (b)). Nonetheless, the B/A-estimator fails to determine the white-noise level, which is included by the R^2-estimator (Fig. 5(c)). The uncertainty is independent of n_{bins} for small $\sigma_{\text{batch}}, \eta$, as shown in Fig. 5(d); the increase of the estimators for greater n_{bins} is attributed to the higher-order effects. It is also notable that the uncertainty is generally closer to the lower limit of the R^2-estimator; therefore, we suggest simply using

$$\sigma(\varphi_{\text{fit}}) \approx \sqrt{\frac{1 - R^2}{R^2 n_{\text{bins}}}} \tag{27}$$

to estimate the experimental uncertainty.

5.3. Effect of the 4ω-component

When the RABBITT signal has a 4ω-component, as shown in Fig. 2, the expected value and variance of φ_{fit} are not affected, according to Eqs. (15) and (19). On the other hand, the
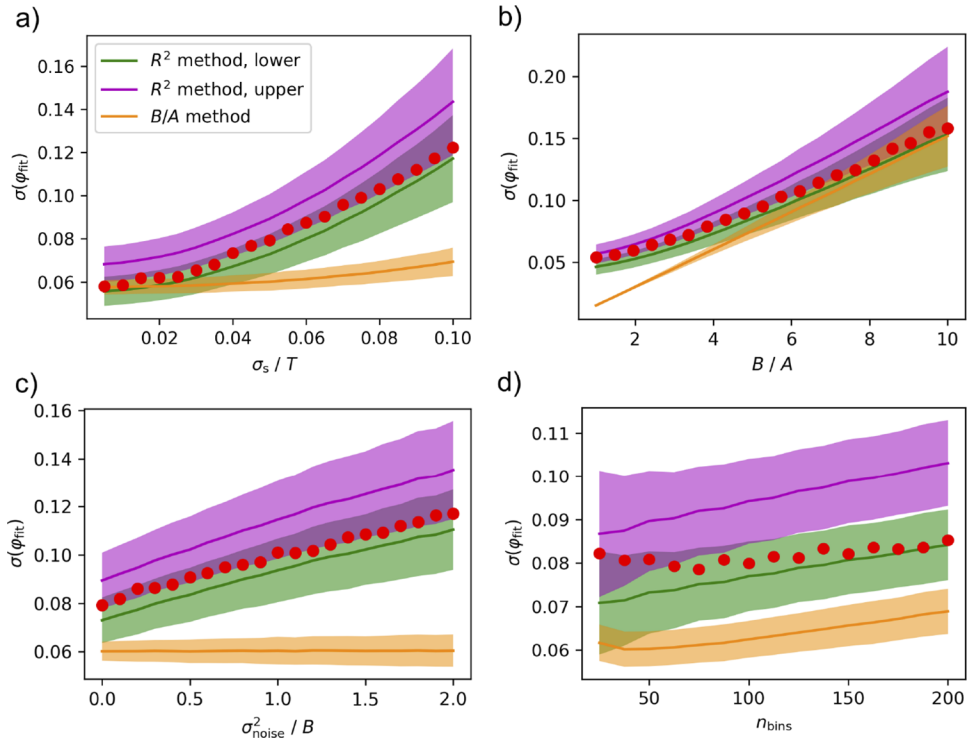
Fig. 5. Simulated RABBITT signals are generated with $N = 10^4$, $B/A = 4.0$, $n_T = 5$, $n_p = 10$, $\sigma_{\text{noise}}^2/B = 0$, and correlated jitter of $\sigma_s/T = 0.05$. (a) Scan over the jitter amplitude. (b) Scan over the B/A ratio. (c) Scan over the relative noise level. (d) Scan over n_p, the correlated jitter $\sigma_{\text{batch}}, s/T = 0.10$ applies on a batch of 50 electrons. Each red circle corresponds to 5000 independent trials.

R^2-value for the 2ω-fitting cannot exceed $A_{2\omega}^2/(A_{2\omega}^2 + A_{4\omega}^2)$, which causes an overestimation of the uncertainty level. The 4ω-effect can be corrected if R^2 is defined based on an extension of Eq. (14):

$$F_{\text{fit}}(t_i) = B_{\text{fit}} + \alpha_2 \cos(2\omega t_i) + \beta_2 \sin(2\omega t_i) + \alpha_4 \cos(4\omega t_i) + \beta_4 \sin(4\omega t_i). \qquad (28)$$

It should be noted that this leads to $R^2 n_{\text{bins}} \sim \chi^2(k = 4)$ for a random signal, which reduces the plateau of the lower limit in Fig. 4(b) to $\sqrt{\pi/8} \approx 0.63$. Therefore, Eq. (28) is suggested to be used only when there is clear evidence of the 4ω-component to avoid artifacts. The numerical simulations are in Supplement 1.

6. Period-fitting uncertainty and spectral leakage in FFT

6.1. Propagation of the period-fitting deviation

So far, we have assumed that the oscillation period is precise. If the fitted period deviates by ΔT from the true value, the fitted phase deviates by (to the lowest order):

$$\Delta\varphi \approx \pi n_T \frac{\Delta T}{T}. \qquad (29)$$

For cosine fitting, the period is retrieved *via* non-linear least-squares fitting of the reference channel. Numerical simulations (see Supplement 1 for details) indicate that

$$\sigma\left(\frac{\Delta T}{T}\right) \approx \frac{0.8}{n_T}\frac{B_{\text{ref}}}{A_{\text{ref}}}\sqrt{\frac{1}{N_{\text{ref}}}}, \tag{30}$$

and thus $\Delta\varphi \sim \mathcal{N}\left(0, 0.64\pi^2/N_{\text{ref}} \cdot B_{\text{ref}}^2/A_{\text{ref}}^2\right)$. Since the same fitted T is applied to all channels, Eq. (29) gives a constant systematic bias; the phase difference between the reference and target channels, however, is unaffected. The uncertainty of the phase difference reads:

$$\sigma(\varphi_{\text{diff}}) = \sqrt{\sigma^2(\varphi_{\text{ref}}) + \sigma^2(\varphi_{\text{tar}})}. \tag{31}$$

On the other hand, the period-fitting error results in a reduction of R^2. For an ideal signal, the effect to the lowest order can be calculated by direct expansion to the lowest order:

$$R^2 \approx 1 - \frac{2 - 3/\pi^2}{6}(\Delta\varphi)^2. \tag{32}$$

Equations (30), (31), and (32) suggest that the period-fitting uncertainty has minor effect when $N_{\text{ref}} \gg N_{\text{tar}}$.

6.2. FFT and spectral leakage

Although FFT uses the same principle of Eq. (14), the fitted period is restricted to an integer fraction of the time range. If a single-frequency signal contains non-integer number of periods, the oscillation is decomposed to all discrete frequencies, which is known as spectral leakage [60], as illustrated in Fig. 6. Here we only take the largest Fourier component, yet it is possible to reconstruct the signal with neighboring components, which results in an envelope, as shown in Ref. [14]. The $\Delta\varphi$ caused by spectral leakage does not affect phase differences, but reduces the R^2-value, and $\Delta\varphi$ does not approach zero when $N_{\text{ref}} \rightarrow \infty$. Hence, the B/A-estimator (Eq. (22)) is preferred, provided that the statistical fluctuation is the main uncertainty source.
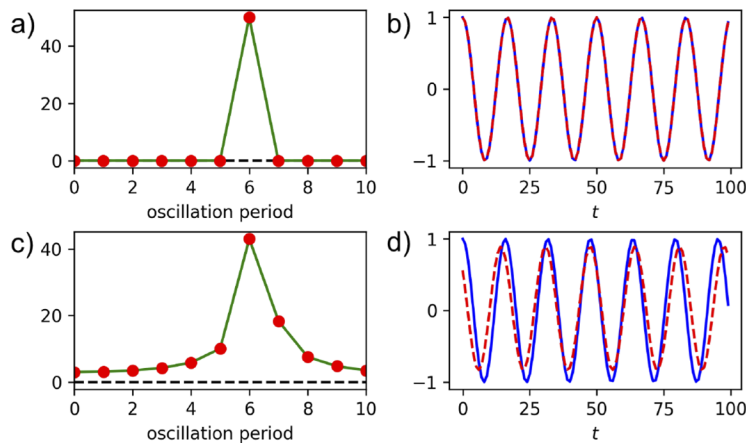

Fig. 6. Illustration of spectral leakage in FFT. (a) and (b) correspond to an ideal sinusoidal signal with exactly 6 periods of oscillation, while (c) and (d) have 6.3 periods of oscillation. (a) and (c) are the FFT spectra (amplitude) of the signals. The time-domain signal (blue solid) and fitted signal (red dashed) in (b) and (d) are based on the non-zero FFT component with the highest amplitude.

7. Weighting scheme

A typical RABBITT experiment is comprised of M individual experiments that are unequal precision measurements with individual uncertainties determined by Eq. (31). Here we suggest the weighting scheme used by the Particle Data Group (PDG) in particle physics [61]:

$$\overline{\varphi} = \frac{\sum_{j=1}^{M} w_j \varphi_j}{\sum_{j=1}^{M} w_j}, \tag{33}$$

where the weight $w_j = 1/\sigma_j^2$. The uncertainty of the weighted mean value is:

$$\sigma_{\mathrm{w}}(\overline{\varphi}) = S' \cdot \left(\sum_{j=1}^{M} w_j \right)^{-1/2}, \quad S' = \max\{S, 1\}, \tag{34}$$

and the χ^2-based factor

$$S = \sqrt{\frac{\sum_{j=1}^{M} (\varphi_j - \overline{\varphi})^2 / \sigma_j^2}{M - 1}} \tag{35}$$

indicates unaddressed uncertainty sources if $S>1$. For $S \leq 1$, the reported uncertainty can be regarded solely from the individual uncertainties. Alternatively, one can use the weighted sample standard deviation:

$$s_{\mathrm{w}}(\overline{\varphi}) = \sqrt{\frac{\sum_{j=1}^{M} w_j (\varphi_j - \overline{\varphi})^2}{(M_{\mathrm{eff}} - 1) \sum_{j=1}^{M} w_j}} = \sqrt{\frac{M - 1}{M_{\mathrm{eff}} - 1}} \cdot S \cdot \left(\sum_{j=1}^{M} w_j \right)^{-1/2}, \tag{36}$$

where $M_{\mathrm{eff}} = \left(\sum_{j=1}^{M} w_j \right)^2 / \left(\sum_{j=1}^{M} w_j^2 \right) \leq M$ is the effective sample size [62], which reflects the inequality of weights. Equation (34) gives the Type B uncertainty in the limit $S' = 1$, whereas Eq. (36) gives the Type A uncertainty if all measurements are given the same weight. Similar formulae for the Type A uncertainties can also be found in Refs. [48–50]. If no systematic shift of the time delay is present among the individual measurements, the two types of uncertainties should be comparable.

8. Examples based on experimental data

Here we present two examples based on the same set of data from the laboratory-frame angular-resolved RABBITT with Ar. The electrons are detected by coincidence measurements using cold target recoil ion momentum spectroscopy (COLTRIMS) [63–65], which pairwise records the 3-dimensional momenta of the photoelectron and photoion, and θ is defined as the angle between the electron ejection and the polarization direction. The two examples show the cases where the discrepancy is dominated by the statistical fluctuation and the variation of experimental conditions, respectively, which is reflected by the S-value.

8.1. Angular-resolved time delays of each sideband

The angular distribution of counts is shown in Fig. 7(a). For each SB, the angular-resolved time delays are referenced to the summed signal over all angles, where negative time delays at higher angles are found (Fig. 7(b), (c)), which agrees with previous studies [32,51,66]. The mean values and uncertainties calculated without weighting or with weighting by Eqs. (34) and (36) are compared in Table 2 and in Supplement 1. $S<1$ indicates that the uncertainty is properly addressed, which indeed explains the discrepancy between individual experiments, although in some regions the uncertainty may be overestimated. Because the electron count rate (~ 2 kHz) is

lower than the repetition rate (5 kHz), indicating that most electrons come from independent shots, and the interval between two counts in the same channel is ~ 1 s, during which jitter already randomizes, the jitter is predominantly uncorrelated and can be treated as smearing effect. Assuming that the background noise is small, the B/A-estimator is applicable, and the results are listed in Supplement 1, where the S-value is typically greater but still less or close to 1. The comparison of time delays obtained from individual experiments can be found in Supplement 1, where the discrepancies are generally well covered by the error bars. Figure 7(b) and (c) compare the results from the two estimators. Neither weighted mean value nor the uncertainty shows a substantial difference.
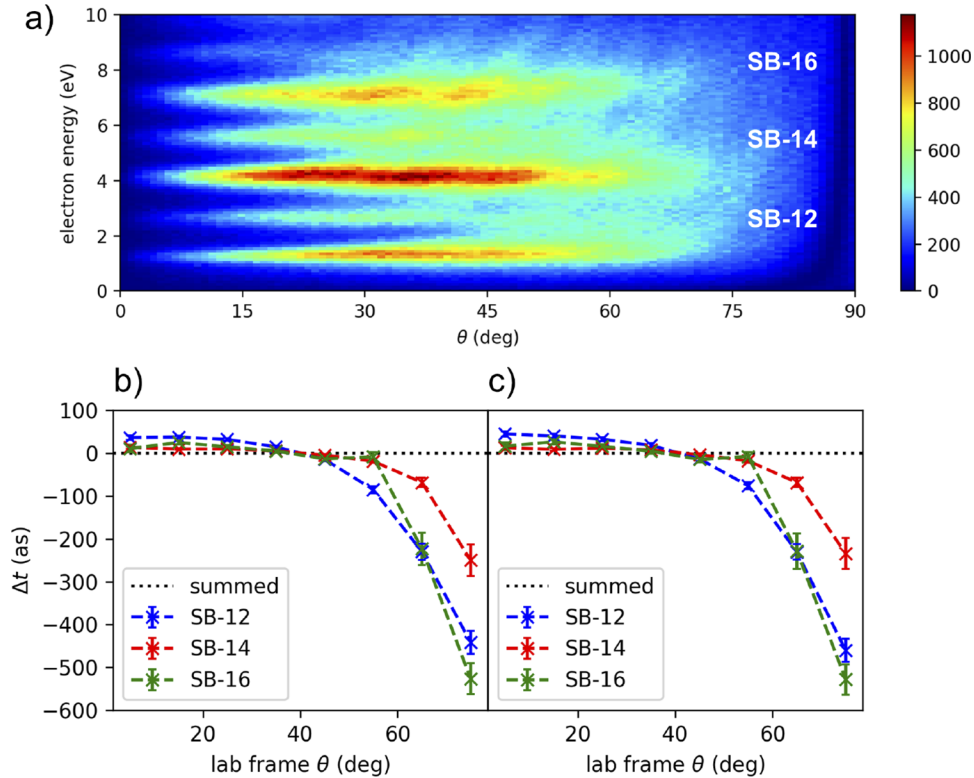

Fig. 7. Angular resolved time delays of Ar in the laboratory frame. (a) shows the signal-strength distribution (summed over all data acquisition times in an individual experiment). (b) and (c) show the relative time delays (referenced to the summed signal over all angles in each SB) based on cosine fitting with uncertainties determined by the B/A ratio and the R^2-value, respectively. The error bars correspond to the uncertainties determined by the PDG method.

8.2. Time delays between sidebands

The phase difference between SBs, as given in Eq. (4), has contributions from both the attochirp (τ_{XUV}) and the atomic time delay (τ_A). Here we focus on the precision of retrieving this total time delay from the experimental data, while the assignment to each component and comparison to theoretical calculations can be found in Ref. [31]. The relative time delays of SBs (with signal summed over all angles and referenced to SB-12) are plotted in Fig. 8; the uncertainties obtained by statistical approach and the R^2-estimator are compared in Table 3 . We have intentionally used all data measured in a period of about one week, including some individual experiments with

Table 2. Angular-resolved time delays for Ar at SB-12 from 18 individual measurements with (w) and without (r) weighting. The weighting is based on the R^2-method

θ range (°)	$\overline{\Delta t_r}$ (as)	$\overline{\Delta t_w}$ (as)	$s_r(\overline{\Delta t})$ (as)	$\sigma_w(\overline{\Delta t})$ (as)	$s_w(\overline{\Delta t})$ (as)	M_{eff}	S
$0 \sim 10$	47.3	44.9	5.8	6.2	5.9	13.3	0.81
$10 \sim 20$	40.2	40.2	4.8	4.7	4.3	11.3	0.71
$20 \sim 30$	32.4	32.6	3.3	4.8	3.8	11.8	0.64
$30 \sim 40$	19.2	18.3	3.1	4.8	2.7	11.6	0.44
$40 \sim 50$	-15.8	-13.4	5.6	5.8	4.3	12.7	0.63
$50 \sim 60$	-82.5	-76.2	13.9	8.3	12.0	7.7	0.91
$60 \sim 70$	-240.0	-230.5	34.2	18.0	24.4	10.3	1.10
$70 \sim 80$	-470.7	-460.1	35.4	27.3	36.2	10.7	1.42

Table 3. Relative time delays of SBs referenced to SB-12 from 18 individual experiments with (w) and without (r) weighting. The weighting is based on the R^2-method

Sideband	$\overline{\Delta t_r}$ (as)	$\overline{\Delta t_w}$ (as)	$s_r(\overline{\Delta t})$ (as)	$\sigma_w(\overline{\Delta t})$ (as)	$s_w(\overline{\Delta t})$ (as)	M_{eff}	S
SB-14	85.3	84.6	11.0	7.5	10.3	10.8	2.25
SB-16	461.6	461.6	34.7	18.1	22.7	11.8	3.69
SB-18	768.6	790.3	28.4	24.5	31.4	11.4	4.22

inappropriate spatial or temporal overlap (e.g. the inset panel of Fig. 8(a)) that yield barely visible oscillations. The estimated uncertainty of these signals are large, and therefore they contribute little to the final result. One can immediately notice that there are outliers with relatively small statistical uncertainties, as compared in Fig. 8(b) and (c), where the relative phases between SB-12 and SB-14 show noticeable differences. The S-values are significantly greater than 1, which means that the discrepancy among individual experiments cannot be fully attributed to the statistical fluctuations and the above-considered effects; this indicates that the attochirp of each individual experiment may not stay constant. This is not surprising, since the gas pressure for HHG was tuned every day to maximize the XUV flux, which is related with the phase matching conditions and has an effect on the pulse structure [67–71]. It agrees with a previous observation
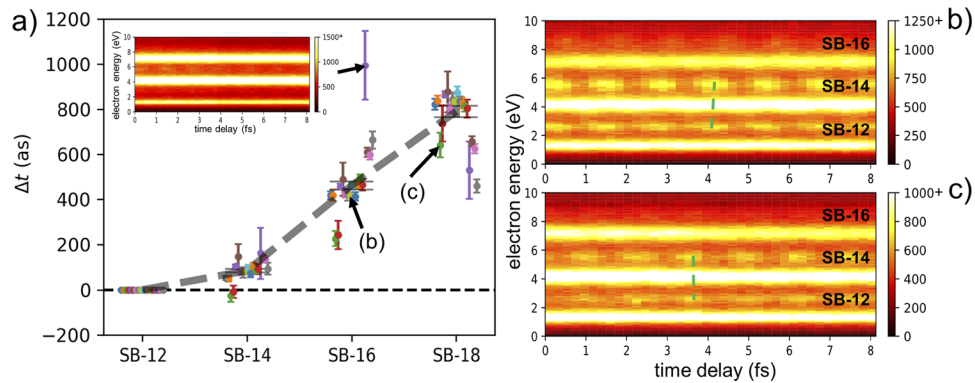

Fig. 8. (a) Relative time delays of SBs (referenced to SB-12) measured by 18 individual experiments (error bars are estimated by the R^2-method and are horizontally displaced to avoid overlap) and their weighted average (bold dashed line, error bar obtained by the PDG method). The beating patterns of 3 individual experiments are shown in the inset of (a), (b), and (c). The green dashed lines in (b) and (c) are guide to the eye.

that the attochirp varies on different days but remains stable during a few hours [31]. Besides, the atomic phase can also be affected by the intensity of the dressing field [72] which varies when the pump-probe overlap changes. Nevertheless, if channels are referenced within the same sideband, as shown in Sec. 8.1, the effect is cancelled, which results in smaller *S*-values.

9. Conclusion

We have shown that the uncertainty of phase retrieval can be extracted along with the fitted phase from the signal *per se* of a single experiment. We have proven that the statistical fluctuation caused by the Poisson distribution of each bin gives $\sigma(\varphi_{\text{fit}}) \approx \frac{B}{A}\sqrt{\frac{2}{N}}$ (the B/A-estimator). This expression is particularly concise, as the binning effect, uncorrelated jitter, and long-term drift are included in the decrease of A (the smearing effect). For a given B/A ratio, the uncertainty is inversely proportional to $\sqrt{N}$.

In order to include the correlated jitter (the shifting effect) and the background noise, the R^2-estimator: $\sigma(\varphi_{\text{fit}}) \approx \sqrt{\frac{1-R^2}{R^2 n_{\text{bins}}}}$ based on the coefficient of determination was proposed. Although it formally depends on n_{bins}, R^2 is also a function of n_{bins}, and the overall ratio is in accordance with the B/A-estimator for the statistical fluctuation. The R^2-estimator, however, is sensitive to the 4ω-component of the signal and the spectral leakage when FFT is applied, while the B/A-estimator is more robust.

Under the assumption that the phase jitter affects the electrons by constant batches (Eq. (13)), we showed that the shifting effect is independent of n_{bins}. If the background noise obeys $\sigma_{\text{noise}}^2 \propto B$, then its contribution to the uncertainty is also independent of n_{bins}. The main effect of the bin width is the binning effect, which reduces the A-value if the bins are too wide; otherwise finer bins do not provide improvement of precision.

A weighting scheme based on the individual uncertainty was proposed, which allows one to combine data of unequal qualities, as illustrated with real experimental data. The *S*-value allows one to check whether the considered uncertainty sources explain the discrepancy among different measurements, as demonstrated by the two examples. When the experimental conditions may alter the expected value of the measured time delay (Sec. 8.2), if one conducts the experiment with better monitoring, the expected outcome will fall on one of those individual experiments, which may deviate from the average of individual experiments under varying conditions. It is therefore suggested to search for the corresponding condition (e.g. HHG gas pressure, dressing field intensity); it not only improves the repeatability and reproducibility, but also potentially leads to new physical insight and discoveries.

Our quantitative uncertainty determination provides a framework of data analysis for future work, which can be extended for the uncertainty analysis of TURTLE fitting and for the two-dimensional energy–time delay RABBITT signal with overlapping or congested bands in the energy domain [36–41]. The related works are in progress.

Disclosures. The authors declare no conflicts of interest.

Data availability. The experimental data presented in this paper are not publicly available at this time but may be obtained from the authors upon reasonable request. The python codes for numerical simulations can be found in Ref. [73] .

Supplemental document. See Supplement 1 for supporting content.

References

1. A. L'Huillier and P. Balcou, "High-order harmonic generation in rare gases with a 1-ps 1053-nm laser," Phys. Rev. Lett. **70**(6), 774–777 (1993).

2. T. Popmintchev, M.-C. Chen, D. Popmintchev, P. Arpin, S. Brown, S. Ališauskas, G. Andriukaitis, T. Balčiunas, O. D. Mücke, A. Pugzlys, A. Baltuška, B. Shim, S. E. Schrauth, A. Gaeta, C. Hernandez-Garcia, L. Plaja, A. Becker, A. Jaron-Becker, M. M. Murnane, and H. C. Kapteyn, "Bright coherent ultrahigh harmonics in the keV x-ray regime from mid-infrared femtosecond lasers," Science **336**(6086), 1287–1291 (2012).

3. P. K. Maroju, C. Grazioli, M. Di Fraia, M. Moioli, D. Ertel, H. Ahmadi, O. Plekan, P. Finetti, E. Allaria, L. Giannessi, G. De Ninno, C. Spezzani, G. Penco, S. Spampinati, A. Demidovich, M. B. Danailov, R. Borghes, G. Kourousias, C. E. Sanches Dos Reis, F. Billé, A. A. Lutman, R. J. Squibb, R. Feifel, P. Carpeggiani, M. Reduzzi, T. Mazza, M. Meyer, S. Bengtsson, N. Ibrakovic, E. R. Simpson, J. Mauritsson, T. Csizmadia, M. Dumergue, S. Kühn, H. Nandiga Gopalakrishna, D. You, K. Ueda, M. Labeye, J. E. Baekhøj, K. J. Schafer, E. V. Gryzlova, A. N. Grum-Grzhimailo, K. C. Prince, C. Callegari, and G. Sansone, "Attosecond pulse shaping using a seeded free-electron laser," Nature **578**(7795), 386–391 (2020).

4. J. Duris, S. Li, T. Driver, E. G. Champenois, J. P. MacArthur, A. A. Lutman, Z. Zhang, P. Rosenberger, J. W. Aldrich, R. Coffee, G. Coslovich, F.-J. Decker, J. M. Glownia, G. Hartmann, W. Helml, A. Kamalov, J. Knurr, J. Krzywinski, M.-F. Lin, J. P. Marangos, M. Nantel, A. Natan, J. T. O'Neal, N. Shivaram, P. Walter, A. L. Wang, J. J. Welch, T. J. A. Wolf, J. Z. Xu, M. F. Kling, P. H. Bucksbaum, A. Zholents, Z. Huang, J. P. Cryan, and A. Marinelli, "Tunable isolated attosecond x-ray pulses with gigawatt peak power from a free-electron laser," Nat. Photonics **14**(1), 30–36 (2020).

5. P. Antoine, A. L'huillier, and M. Lewenstein, "Attosecond pulse trains using high–order harmonics," Phys. Rev. Lett. **77**(7), 1234–1237 (1996).

6. P.-M. Paul, E. S. Toma, P. Breger, G. Mullot, F. Augé, P. Balcou, H. G. Muller, and P. Agostini, "Observation of a train of attosecond pulses from high harmonic generation," Science **292**(5522), 1689–1692 (2001).

7. M. Hentschel, R. Kienberger, C. Spielmann, G. A. Reider, N. Milosevic, T. Brabec, P. Corkum, U. Heinzmann, M. Drescher, and F. Krausz, "Attosecond metrology," Nature **414**(6863), 509–513 (2001).

8. H. G. Muller, "Reconstruction of attosecond harmonic beating by interference of two-photon transitions," Appl. Phys. B **74**(S1), s17–s21 (2002).

9. Y. Mairesse, A. de Bohan, L. J. Frasinski, H. Merdji, L. C. Dinu, P. Monchicourt, P. Breger, M. Kovacev, R. Taïeb, B. Carré, H. G. Muller, P. Agostini, and P. Salières, "Attosecond synchronization of high-harmonic soft x-rays," Science **302**(5650), 1540–1543 (2003).

10. S. Haessler, J. Caillat, W. Boutu, C. Giovanetti-Teixeira, T. Ruchon, T. Auguste, Z. Diveki, P. Breger, A. Maquet, B. Carré, R. Taïeb, and P. Salières, "Attosecond imaging of molecular electronic wavepackets," Nat. Phys. **6**(3), 200–206 (2010).

11. K. Klünder, J. M. Dahlström, M. Gisselbrecht, T. Fordell, M. Swoboda, D. Guénot, P. Johnsson, J. Caillat, J. Mauritsson, A. Maquet, Taïeb, and A. L'Huillier, "Probing single-photon ionization on the attosecond time scale," Phys. Rev. Lett. **106**(14), 143002 (2011).

12. J. Itatani, F. Quéré, G. L. Yudin, M. Y. Ivanov, F. Krausz, and P. B. Corkum, "Attosecond streak camera," Phys. Rev. Lett. **88**(17), 173903 (2002).

13. Y. Mairesse and F. Quéré, "Frequency-resolved optical gating for complete reconstruction of attosecond bursts," Phys. Rev. A **71**(1), 011401 (2005).

14. L. Cattaneo, J. Vos, M. Lucchini, L. Gallmann, C. Cirelli, and U. Keller, "Comparison of attosecond streaking and RABBITT," Opt. Express **24**(25), 29060–29076 (2016).

15. M. Schultze, M. Fiess, N. Karpowicz, J. Gagnon, M. Korbman, M. Hofstetter, S. Neppl, A. L. Cavalieri, Y. Komninos, T. Mercouris, C. A. Nicolaides, R. Pazourek, S. Nägele, J. Feist, J. Burgdörfer, A. M. Azzeer, R. Ernstorfer, R. Kienberger, U. Kleineberg, E. Goulielmakis, F. Krausz, and V. S. Yakovlev, "Delay in photoemission," Science **328**(5986), 1658–1662 (2010).

16. M. Chini, S. Gilbertson, S. D. Khan, and Z. Chang, "Characterizing ultrabroadband attosecond lasers," Opt. Express **18**(12), 13006–13016 (2010).

17. N. Dudovich, O. Smirnova, J. Levesque, M. Ivanov, D. M. Villeneuve, and P. B. Corkum, "Measuring and controlling the birth of attosecond pulses," Nat. Phys. **2**(11), 781–786 (2006).

18. V. Véniard, R. Taïeb, and A. Maquet, "Phase dependence of (n+1)-color (n>1) IR-UV photoionization of atoms with higher harmonics," Phys. Rev. A **54**(1), 721–728 (1996).

19. J. Dahlström, A. L'Huillier, and A. Maquet, "Introduction to attosecond delays in photoionization," J. Phys. B: At., Mol. Opt. Phys. **45**(18), 183001 (2012).

20. J. M. Dahlström, D. Guénot, K. Klünder, M. Gisselbrecht, J. Mauritsson, A. L'Huillier, A. Maquet, and R. Taïeb, "Theory of attosecond delays in laser-assisted photoionization," Chem. Phys. **414**, 53–64 (2013).

21. D. Bharti, D. Atri-Schuller, G. Menning, K. R. Hamilton, R. Moshammer, T. Pfeifer, N. Douguet, K. Bartschat, and A. Harth, "Decomposition of the transition phase in multi-sideband schemes for reconstruction of attosecond beating by interference of two-photon transitions," Phys. Rev. A **103**(2), 022834 (2021).

22. A. Tonomura, J. Endo, T. Matsuda, T. Kawasaki, and H. Ezawa, "Demonstration of single-electron buildup of an interference pattern," Am. J. Phys. **57**(2), 117–120 (1989).

23. M. Swoboda, J. Dahlström, T. Ruchon, P. Johnsson, J. Mauritsson, A. L'Huillier, and K. Schafer, "Intensity dependence of laser-assisted attosecond photoionization spectra," Laser Phys. **19**(8), 1591–1599 (2009).

24. V. Loriot, A. Marciniak, G. Karras, B. Schindler, G. Renois-Predelus, I. Compagnon, B. Concina, R. Brédy, G. Celep, C. Bordas, E. Constant, and F. Lépine, "Angularly resolved RABBITT using a second harmonic pulse," J. Opt. **19**(11), 114003 (2017).

25. A. Harth, R. Moshammer, T. Pfeifer, K. Bartschat, and N. Douguet, "Extracting phase information on continuum-continuum couplings," Phys. Rev. A **99**(2), 023410 (2019).

26. G. Laurent, W. Cao, H. Li, Z. Wang, I. Ben-Itzhak, and C. L. Cocke, "Attosecond control of orbital parity mix interferences and the relative phase of even and odd harmonics in an attosecond pulse train," Phys. Rev. Lett. **109**(8), 083001 (2012).

27. M. Bertolino and J. M. Dahlström, "Multiphoton interaction phase shifts in attosecond science," Phys. Rev. Res. **3**(1), 013270 (2021).

28. D. Kiesewetter, R. R. Jones, A. Camper, S. B. Schoun, P. Agostini, and L. F. DiMauro, "Probing electronic binding potentials with attosecond photoelectron wavepackets," Nat. Phys. **14**(1), 68–73 (2018).

29. S. Kazamias and P. Balcou, "Intrinsic chirp of attosecond pulses: Single-atom model versus experiment," Phys. Rev. A **69**(6), 063416 (2004).

30. K. Varjú, Y. Mairesse, P. Agostini, P. Breger, B. Carré, L. J. Frasinski, E. Gustafsson, P. Johnsson, J. Mauritsson, H. Merdji, P. Monchicourt, A. L'Huillier, and P. Salières, "Reconstruction of attosecond pulse trains using an adiabatic phase expansion," Phys. Rev. Lett. **95**(24), 243901 (2005).

31. C. Palatchi, J. M. Dahlström, A. S. Kheifets, I. A. Ivanov, D. M. Canaday, P. Agostini, and L. F. DiMauro, "Atomic delay in helium, neon, argon and krypton," J. Phys. B: At., Mol. Opt. Phys. **47**(24), 245003 (2014).

32. A. W. Bray, F. Naseem, and A. S. Kheifets, "Simulation of angular-resolved RABBITT measurements in noble-gas atoms," Phys. Rev. A **97**(6), 063404 (2018).

33. G. Schmid, K. Schnorr, S. Augustin, S. Meister, H. Lindenblatt, F. Trost, Y. Liu, N. Stojanovic, A. Al-Shemmary, T. Golz, R. Treusch, M. Gensch, M. Kübel, L. Foucar, A. Rudenko, J. Ullrich, C. D. Schröter, T. Pfeifer, and R. Moshammer, "Terahertz-field-induced time shifts in atomic photoemission," Phys. Rev. Lett. **122**(7), 073001 (2019).

34. J. Fuchs, N. Douguet, S. Donsa, F. Martin, J. Burgdörfer, L. Argenti, L. Cattaneo, and U. Keller, "Time delays from one-photon transitions in the continuum," Optica **7**(2), 154–161 (2020).

35. M. Isinger, D. Busto, S. Mikaelsson, S. Zhong, C. Guo, P. Salières, C. Arnold, A. l'Huillier, and M. Gisselbrecht, "Accuracy and precision of the RABBITT technique," Phil. Trans. R. Soc. A **377**(2145), 20170475 (2019).

36. V. Gruson, L. Barreau, Á. Jiménez-Galan, F. Risoud, J. Caillat, A. Maquet, B. Carré, F. Lepetit, J.-F. Hergott, T. Ruchon, L. Argenti, R. Taïeb, F. Martín, and P. Salières, "Attosecond dynamics through a Fano resonance: Monitoring the birth of a photoelectron," Science **354**(6313), 734–738 (2016).

37. D. Busto, L. Barreau, M. Isinger, M. Turconi, C. Alexandridi, A. Harth, S. Zhong, R. J. Squibb, D. Kroon, S. Plogmaker, M. Miranda, Á. Jiménez-Galán, L. Argenti, C. L. Arnold, R. Feifel, F. Martin, M. Gisselbrecht, A. L'Huillier, and P. Salières, "Time–frequency representation of autoionization dynamics in helium," J. Phys. B: At., Mol. Opt. Phys. **51**(4), 044002 (2018).

38. A. Kamalov, A. L. Wang, P. H. Bucksbaum, D. J. Haxton, and J. P. Cryan, "Electron correlation effects in attosecond photoionization of CO_2," Phys. Rev. A **102**(2), 023118 (2020).

39. I. Jordan and H. J. Wörner, "Extracting attosecond delays from spectrally overlapping interferograms," J. Opt. **20**(2), 024013 (2018).

40. A. Jain, T. Gaumnitz, A. Bray, A. Kheifets, and H. J. Wörner, "Photoionization delays in xenon using single-shot referencing in the collinear back-focusing geometry," Opt. Lett. **43**(18), 4510–4513 (2018).

41. I. Jordan, M. Huppert, D. Rattenbacher, M. Peper, D. Jelovina, C. Perry, A. von Conta, A. Schild, and H. J. Wörner, "Attosecond spectroscopy of liquid water," Science **369**(6506), 974–979 (2020).

42. JCGM, "Evaluation of measurement data–guide to the expression of uncertainty in measurement," Document produced by Working Group 1 of the Joint Committee for Guides in Metrology (JCGM/WG 1) (2008).

43. B. N. Taylor and C. E. Kuyatt, *Guidelines for evaluating and expressing the uncertainty of NIST measurement results* (US Department of Commerce, Technology Administration, National Institute of Standards and Technology, 1994).

44. W. Kessel, "Measurement uncertainty according to ISO/BIPM-GUM," Thermochim. Acta **382**(1-2), 1–16 (2002).

45. M. Huppert, I. Jordan, D. Baykusheva, A. von Conta, and H. J. Wörner, "Attosecond delays in molecular photoionization," Phys. Rev. Lett. **117**(9), 093001 (2016).

46. I. Jordan, M. Huppert, S. Pabst, A. S. Kheifets, D. Baykusheva, and H. J. Wörner, "Spin-orbit delays in photoemission," Phys. Rev. A **95**(1), 013404 (2017).

47. A. Jain, T. Gaumnitz, A. Kheifets, and H. J. Wörner, "Using a passively stable attosecond beamline for relative photoemission time delays at high XUV photon energies," Opt. Express **26**(22), 28604–28620 (2018).

48. S. Nandi, E. Plésiat, S. Zhong, A. Palacios, D. Busto, M. Isinger, L. Neoričić, C. L. Arnold, R. J. Squibb, R. Feifel, P. Decleva, A. L'Huillier, F. Martín, and M. Gisselbrecht, "Attosecond timing of electron emission from a molecular shape resonance," Sci. Adv. **6**(31), eaba7762 (2020).

49. S. Zhong, J. Vinbladh, D. Busto, R. J. Squibb, M. Isinger, L. Neoričić, H. Laurell, R. Weissenbilder, C. L. Arnold, R. Feifel, J. M. Dahlström, G. Wendin, M. Gisselbrecht, E. Lindroth, and A. L'Huillier, "Attosecond electron–spin dynamics in Xe 4d photoionization," Nat. Commun. **11**(1), 5042–5046 (2020).

50. C. Alexandridi, D. Platzer, L. Barreau, D. Busto, S. Zhong, M. Turconi, L. Neoričić, H. Laurell, C. L. Arnold, A. Borot, J.-F. Hergott, O. Tcherbakoff, M. Lejman, M. Gisselbrecht, E. Lindroth, A. L'Huillier, J. M. Dahlström, and P. Salières, "Attosecond photoionization dynamics in the vicinity of the Cooper minima in argon," Phys. Rev. Res. **3**(1), L012012 (2021).

51. J. Joseph, F. Holzmeier, D. Bresteau, C. Spezzani, T. Ruchon, J. F. Hergott, O. Tcherbakoff, P. D'Oliveira, J. C. Houver, and D. Dowek, "Angle-resolved studies of XUV–IR two-photon ionization in the RABBITT scheme," J. Phys. B: At., Mol. Opt. Phys. **53**(18), 184007 (2020).

52. G. Bohm and G. Zech, *Introduction to statistics and data analysis for physicists* (DESY Hamburg, 2010), pp. 16–20, 66–72, 94–98.

53. C. Bourassin-Bouchet, L. Barreau, V. Gruson, J.-F. Hergott, F. Quéré, P. Salières, and T. Ruchon, "Quantifying decoherence in attosecond metrology," Phys. Rev. X **10**(3), 031048 (2020).

54. G. Foster, J. Fixler, J. McGuirk, and M. Kasevich, "Method of phase extraction between coupled atom interferometers using ellipse-specific fitting," Opt. Lett. **27**(11), 951–953 (2002).

55. C. Krüger, J. Fuchs, L. Cattaneo, and U. Keller, "Attosecond resolution from free running interferometric measurements," Opt. Express **28**(9), 12862–12871 (2020).

56. See the supplementary information for general formulae, additional numerical simulations, experimental descriptions, and angular-resolved time delays for other sidebands. https://doi.org/10.6084/m9.figshare.15039294

57. T. O. Kvålseth, "Cautionary note about R^2," The Am. Stat. **39**(4), 279–285 (1985).

58. G. Casella and C. P. Robert, "Rao-blackwellisation of sampling schemes," Biometrika **83**(1), 81–94 (1996).

59. J. Schoukens and J. Renneboog, "Modeling the noise influence on the Fourier coefficients after a discrete Fourier transform," *IEEE transactions on instrumentation and measurement* pp. 278–286 (1986).

60. F. J. Harris, "On the use of windows for harmonic analysis with the discrete Fourier transform," Proc. IEEE **66**(1), 51–83 (1978).

61. L. Montanet, K. Gieselmann, R. M. Barnett, D. E. Groom, T. G. Trippe, C. G. Wohl, B. Armstrong, G. S. Wagman, H. Murayama, J. Stone, J. J. Hernandez, F. C. Porter, R. J. Morrison, A. Manohar, M. Aguilar-Benitez, C. Caso, P. Lantero, R. L. Crawford, M. Roos, N. A. Törnqvist, K. G. Hayes, G. Höhler, S. Kawabata, D. M. Manley, K. Olive, R. E. Shrock, S. Eidelman, R. H. Schindler, A. Gurtu, K. Hikasa, G. Conforto, R. L. Workman, and C. Grab, "Review of particle properties," Phys. Rev. D **50**(3), 1173–1814 (1994).

62. L. Kish, "Weighting for unequal P_i," J. Off. Stat. **8**, 183–200 (1992).

63. R. Dörner, V. Mergel, O. Jagutzki, L. Spielberger, J. Ullrich, R. Moshammer, and H. Schmidt-Böcking, "Cold target recoil ion momentum spectroscopy: a "momentum microscope" to view atomic collision dynamics," Phys. Rep. **330**(2-3), 95–192 (2000).

64. J. Ullrich, R. Moshammer, A. Dorn, R. Dörner, L. P. H. Schmidt, and H. Schmidt-Böcking, "Recoil-ion and electron momentum spectroscopy: reaction-microscopes," Rep. Prog. Phys. **66**(9), 1463–1545 (2003).

65. M. Sabbar, S. Heuser, R. Boge, M. Lucchini, L. Gallmann, C. Cirelli, and U. Keller, "Combining attosecond XUV pulses with coincidence spectroscopy," Rev. Sci. Instrum. **85**(10), 103113 (2014).

66. C. Cirelli, C. Marante, S. Heuser, C. L. M. Petersson, Á. J. Galán, L. Argenti, S. Zhong, D. Busto, M. Isinger, S. Nandi, S. Maclot, L. Rading, P. Johnsson, M. Gisselbrecht, M. Lucchini, L. Gallmann, J. M. Dahlström, E. Lindroth, A. L'Huillier, F. Martín, and U. Keller, "Anisotropic photoemission time delays close to a Fano resonance," Nat. Commun. **9**(1), 955–959 (2018).

67. E. Constant, D. Garzella, P. Breger, E. Mével, C. Dorrer, C. Le Blanc, F. Salin, and P. Agostini, "Optimizing high harmonic generation in absorbing gases: Model and experiment," Phys. Rev. Lett. **82**(8), 1668–1671 (1999).

68. L. Van Dao, S. Teichmann, and P. Hannaford, "Phase-matching for generation of few high order harmonics in a semi-infinite gas cell," Phys. Lett. A **372**(31), 5254–5257 (2008).

69. D. S. Steingrube, T. Vockerodt, E. Schulz, U. Morgner, and M. Kovačev, "Phase matching of high-order harmonics in a semi-infinite gas cell," Phys. Rev. A **80**(4), 043819 (2009).

70. S. Kazamias, S. Daboussi, O. Guilbaud, K. Cassou, D. Ros, B. Cros, and G. Maynard, "Pressure-induced phase matching in high-order harmonic generation," Phys. Rev. A **83**(6), 063405 (2011).

71. X.-Y. Li, G.-L. Wang, and X.-X. Zhou, "Effects of pressure and gas-jet thickness on the generation of attosecond pulse," Chin. Phys. B **23**(1), 013102 (2014).

72. J. Mauritsson, M. B. Gaarde, and K. J. Schafer, "Accessing properties of electron wave packets generated by attosecond pulse trains through time-dependent calculations," Phys. Rev. A **72**(1), 013401 (2005).

73. J.-B. Ji, "Codes for "Quantitative uncertainty determination of phase retrieval in RABBITT"," zenodo (2021), https://doi.org/10.5281/zenodo.4762049.